**TECHNICAL NOTE**

# Optimum delineation of skin structure for dose calculation with the linear Boltzmann transport equation algorithm in radiotherapy treatment planning

Keisuke Hamada[1,2] · Toshioh Fujibuchi[3] · Hiroyuki Arakawa[3]

## Abstract

This study investigated the effectiveness of placing skin-ring structures to enhance the precision of skin dose calculations in patients who had undergone head and neck volumetric modulated arc therapy using the Acuros XB algorithm. The skin-ring structures in question were positioned 2 mm below the skin surface (skin A) and 1 mm above and below the skin surface (skin B) within the treatment-planning system. These structures were then tested on both acrylic cylindrical and anthropomorphic phantoms and compared with the Gafchromic EBT3 film (EBT3). The results revealed that the maximum dose differences between skins A and B for the cylindrical and anthropomorphic phantoms were approximately 12% and 2%, respectively. In patients 1 and 2, the dose differences between skins A and B were 9.2% and 8.2%, respectively. Ultimately, demonstrated that the skin-dose calculation accuracy of skin B was within 2% and did not impact the deep organs.

**Keywords** Skin-surface dose · Skin-ring structure · Volumetric modulated arc therapy · Acuros XB · Head and neck

## 1 Introduction

Acute radiation dermatitis (ARD) is a common adverse effect observed in patients undergoing radiation therapy for head and neck cancer [1]. The number of ARD cases has decreased due to advancements in irradiation technology, specifically the shift from three-dimensional conformal radiotherapy to volumetric modulated arc therapy (VMAT) [2–4]. However, ARD still occurs in many patients, and there have been reports of severe cases [1, 5]. Therefore, accurate skin-dose calculations using treatment-planning systems (TPSs) are crucial. Currently, there are no available radiotherapy guidelines for assessing skin doses [6]. As a result, skin doses are not evaluated using a dose–volume histogram.

The skin-dose evaluation lacks a defined ring structure due to the inaccuracies found in calculations based on the percentage depth dose for photon beams from a single direction [7, 8]. However, with the introduction of VMAT irradiation technology, the skin is now exposed to radiation from multiple directions, and it is important to investigate the damage caused to the skin as it is affected by both the incoming and outgoing directions. In this study, we compared the dose measured from the Gafchromic EBT3 film (EBT3) with the dose calculated using the TPS, examined the dose gradient at the skin–air interface, and investigated the average dose in the target volume and organs at risk.

## 2 Materials and methods

### 2.1 Contour definition of the skin structure and verification conditions

Skin A was the default setting in Eclipse version 13.6 (Varian Medical Systems, Palo Alto, CA, USA), where the external body contour was automatically constructed after importing computed tomography (CT) images. Skin A had

✉ Keisuke Hamada
hamada.keisuke.we@mail.hosp.go.jp

1   Department of Radiological Technology, National Hospital Organization Kagoshima Medical Center, 8-1 Shiroyama-cho, Kagoshima 892-0853, Japan

2   Department of Health Sciences, Graduate School of Medicine, Kyushu University, Fukuoka, Japan

3   Department of Health Sciences, Faculty of Medical Sciences, Kyushu University, Fukuoka, Japan

a thickness of 2 mm and was obtained from the skin surface as described in previous studies [9, 10] (Fig. 1a, b). Skin dose calculations for the TPS were only performed inside the body contour [11, 12]. In skin B, the skin surface was located at the center of the skin ring structure. Skin B had a 1-mm structure in front of and behind the skin surface. The external body contour included skin B, extending 1 mm outward from the default settings (Fig. 1c, d). The extension of the external body contour included an air layer on the skin surface. Notably, thermoplastic masks and couches can significantly affect the skin dose of a patient [13–15]. Therefore, these were included in the external body contour to measure the effect of scattered radiation [11].

To create skins A and B, the TPS used the "extract wall" function to create a skin-ring structure. A structural functional margin was used to extend the external body contours. The treatment data from two patients were fused to an acrylic cylindrical phantom in Fig. 2 and anthropomorphic

phantoms in Fig. 3 (QUART, Zorneding, Germany) using the TPS. The cylindrical phantom had a diameter of 12 cm and length of 15 cm, representing the neck area. The photon energy used was 6 MV, the calculation algorithm was Eclipse version 13.6 Acuros XB (AXB), and the calculation grid size was 1.5 mm. Treatment-planning CT images with a slice thickness of 2 mm were imported into the TPS. CT was performed using SOMATOM Definition AS 64 Open (Siemens Healthineers, Erlangen, Germany). The field of view of the CT images was 500 mm, and the pixel size was 0.9765 mm.

## 2.2 Target volume, organs at risk, and planned organ-risk volume

Contouring and plan optimization are briefly summarized here, with a more detailed description available in the literature [16, 17]. The target volumes were defined as shown
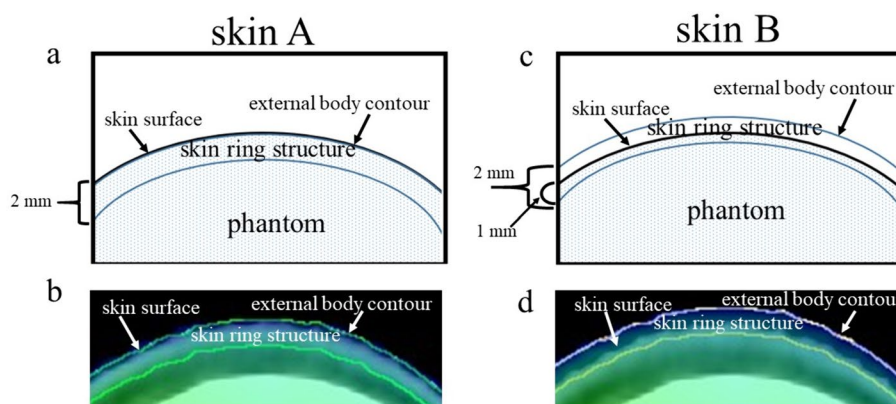


**Fig. 1** **a** Skin A is a skin-ring structure located 2 mm below the skin surface. The external body contour is contoured at the same location as the skin surface with default settings. **b** Dose distribution in skin A and the skin surface of the treatment-planning system. The doses are calculated at a depth of 2 mm from the skin surface. **c** Skin B is a 2-mm skin-ring structure with its center on the skin surface. The external body contour is extended outward by 1 mm. **d** Dose distribution in skin B and the skin surface of the treatment-planning system



**Fig. 2** **a** Acrylic cylindrical phantom simulating the neck. **b** TPS calculation conditions and the measurement position of the EBT3 film are shown. The cylindrical phantom has a diameter of 12 cm and length of 15 cm. The measured doses from the EBT3 film and the calculated doses from the TPS are compared at the same location on the acrylic cylindrical phantom. TPS, treatment-planning system; EBT3, Gafchromic EBT3 film
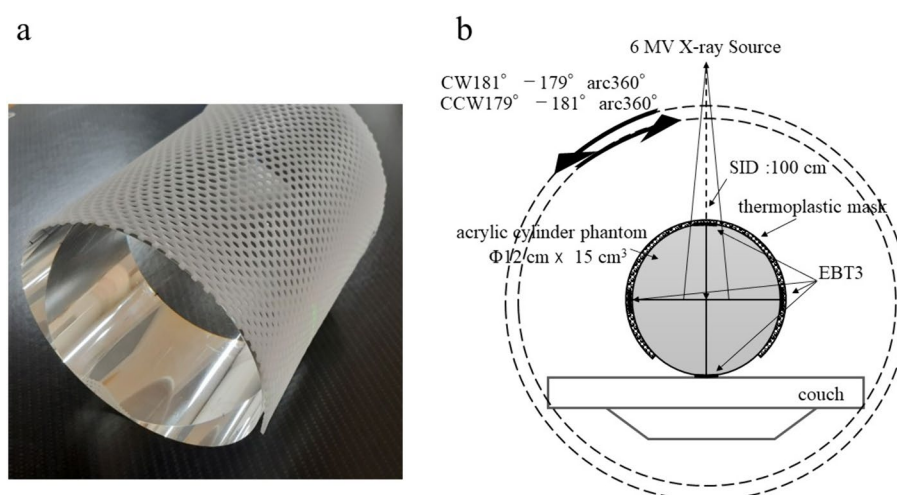
**Fig. 3 a** Anthropomorphic phantom covered with a thermoplastic mask. **b** Skin-ring structure of the TPS and location of the EBT3 film. (1) Right parotid gland, (2) chin, (3) left parotid gland, (4) right clavicle, (5) sternum pattern, and (6) left clavicle. TPS, treatment-planning system; EBT3, Gafchromic EBT3 film
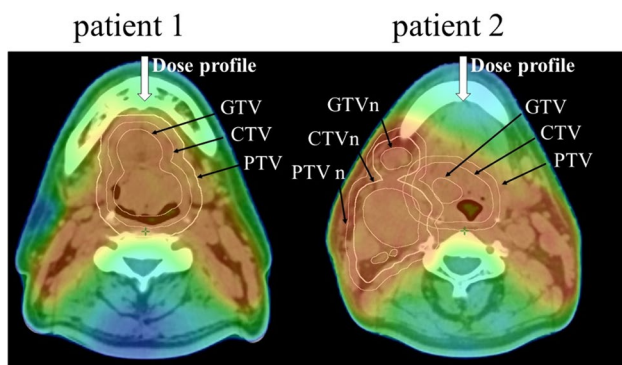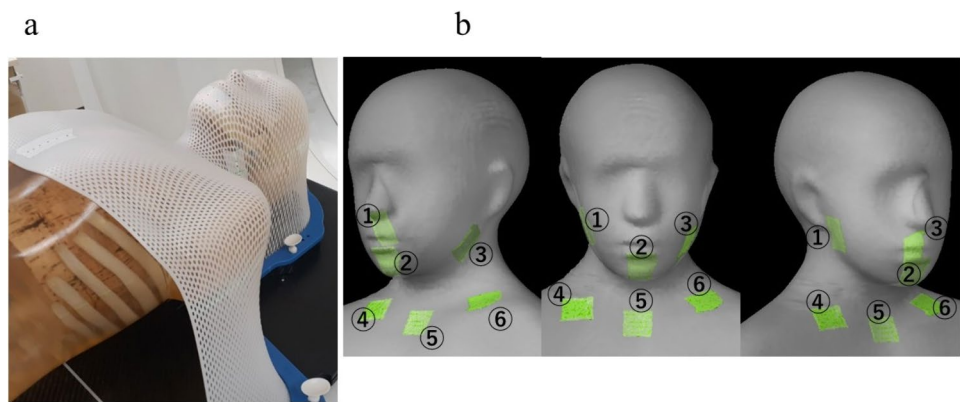


**Fig. 4** Patient 1 is a stage II patient with a T2, N0, and M0 TNM classification for oropharyngeal cancer. Patient 2 is a stage I patient with a T1, N1, and M0 TNM classification for oropharyngeal cancer. The target volume and dose distribution are shown. A 2-mm portion of the PTVn in patient 2 is excluded from the skin surface. Dose profiles are calculated at the arrow positions. PTVn, planning target volume of potentially metastatic lymph node enlargement

in Fig. 4. The gross tumor volume (GTV) included the gross extent of the primary disease and lymph-node metastases, taking into account clinical and radiologic findings. The clinical target volume (CTV) was defined as the GTV plus a 5-mm margin, considering anatomic and clinical oncologic features. The planning target volume (PTV) was defined as the CTV plus a 5-mm margin. To prevent a skin overdose, a 2-mm exclusion zone was created around the PTV, assuming no sacrifice in CTV dose.

Gross enlarged lymph nodes (GTVns) with potential for metastasis were defined based on clinical and radiologic findings. The CTV of potentially metastatic lymph nodes (CTVns) included the GTVn plus a 5 mm margin, considering anatomic and clinical oncologic features. The PTV of potentially metastatic lymph-node enlargement (PTVn) was defined as the CTVn plus a 5-mm margin. The organs at risk included the skin, brain, brainstem, lungs, spinal cord, right parotid gland, left parotid gland, trachea,

brainstem, planned organ-risk volume (PRV), spinal cord PRV, right parotid PRV, and left parotid PRV.

## 2.3 Gafchromic film EBT3 dosimetry

EBT3 is a reliable instrument for skin dosimetry [18, 19]. The irradiated EBT3 (Ashland Inc., Bridgewater, NJ, USA) was read 24 h later using an EPSON ES-10000G flat-head scanner (Seiko Epson Corporation, Suwa, Nagano, Japan). The films were individually placed at the center of the scanner. Film data were analyzed using Dose-Difference Analysis version 14 (R-TEC Inc., Itabashi, Tokyo, Japan). To ensure measurement reliability, the data were obtained from three separate irradiations under identical conditions, and the average value was used. The EBT3 was carefully placed in close contact with an anthropomorphic phantom, as depicted in Fig. 3. For the anthropomorphic phantoms, a 1.6-mm thick thermoplastic mask (CIVCO Radiotherapy, Orange City, IA, USA) with a 4-mm diameter hole was employed. A 1-mm spherical plastic was positioned at each of the four corners of the EBT3 as a landmark, corresponding to the TPS skin-ring structure. The analysis of EBT3 was performed using *D-D* Analysis version 14. The region of interest and the skin-ring structure for EBT3 were 2.5 cm long and 3 cm wide. EBT3 had a three-phase structure with a thickness of 0.278 mm.

## 2.4 Comparison of the measured dose of EBT3 and the calculated dose of TSP

This section compares the dosimetry of the EBT3 and TPS calculations for cylindrical and anthropomorphic phantoms in patients 1 and 2. The TPS contour tool was used to create a skin-ring structure with dimensions of 2.5 cm length and 3 cm width on both the cylindrical and anthropomorphic phantoms. The ring structures on the TPS were referred to as skins A and B (Fig. 1). The positions of the TPS calculations and EBT3 measurements were the same. A thermoplastic mask was applied to the phantom. The EBT3 and TPS were

placed at four locations on the cylindrical phantom: upper to 0° beam angle, left to 90° beam angle, bottom to 180° beam angle, and right to 270° beam angle (Fig. 2). In the anthropomorphic phantom, the EBT3 and TPS structures were placed at six arbitrary locations: right parotid gland, chin, left parotid gland, right clavicle, left clavicle, and sternal pattern (Fig. 3).

The TPS and EBT3 doses were compared using Eq. (1).

$$\text{Difference}\,(\%) = \{(D_{\text{TPS}} - D_{\text{EBT3}})/D_{\text{EBT3}}\} \times 100, \cdots, \quad (1)$$

where $D_{\text{TPS}}$ represents the TPS dose and $D_{\text{EBT3}}$ represents the EBT3 dose.

### 2.5 Dose gradient at the skin–air interface

The skin–air interface of various skin-ring structure arrangements was examined. The skin–air interface dose profiles for patients 1 and 2 were examined by selecting the location with the largest GTV diameter and the steepest dose gradient that strongly dose constrains the dose (Fig. 4). The clinical irradiation conditions included a dose of 2.0 Gy per session, a total of 35 sessions, and a total dose of 70 Gy administered five times per week.

### 2.6 Comparison of the target volume mean dose, risk-organ mean doses, and planned organ-risk volume

The target volumes of skins A and B, as well as the doses to normal organs, were investigated in patients 1 and 2. In patient 1, the skin, GTV, CTV, and PTV were investigated, while in patient 2, the investigation included the skin, GTV, CTV, PTV, GTVn, CTVn, and PTVn. The organs at risk included the skin, brain, brainstem, lungs, spinal cord, right

and left parotid glands, trachea, brainstem PRV, spinal cord PRV, right parotid PRV, and left parotid PRV. The dose to the skin-ring structure, the average dose to the target volume, and the average dose to the organs at risk for skins A and B were compared using Eq. (2).

$$\text{Difference}\,(\%) = \{(\text{skin}\,A - \text{skin}\,B)/\text{skin}\,A\} \times 100, \cdots. \quad (2)$$

## 3 Results

### 3.1 Comparison between the measured dose of EBT3 and the calculated dose of TSP

Figure 5 shows the results of irradiating a cylindrical phantom. The maximum and minimum dose differences between skin A and EBT3 were 12.5% and 2.72%, respectively. The dose difference between skin B and EBT3 was approximately 2.0%. The bottom of the cylindrical phantom showed a small dose difference of 1% (skin A) to 2% (skin B) with EBT3. A comparison between the EBT3 dose and TPS dose calculations for anthropomorphic phantoms showed a maximum difference of 13.4% and a minimum of 6.27% for skin A and within approximately ± 2.0% for skin B (Fig. 6). Skin B matched the EBT3 dose, regardless of the measurement site.

### 3.2 Dose gradient at the skin–air interface

The dose gradients at the skin–air interfaces for patients 1 and 2 are shown in Fig. 7a and b, respectively. Dose gradients differed between skin A and B in patient 1. For skin A, the dose calculation began 3.0 mm outside the skin surface (Fig. 7a (1)), and the dose increased by approximately 600 cGy for



**Fig. 5** Comparison between EBT3-measured doses and TPS-calculated doses for skin A and B in a cylindrical phantom. For skin A, the TPS-calculated doses are higher than those measured by EBT3. In contrast, the dose difference for skin B is within 2% of the EBT3 measurements. In addition, for skin A, the dose difference between TPS and EBT3 is smaller at the bottom of the phantom compared to the top, right, and left sides. TPS, treatment planning system; EBT3, Gafchromic EBT3 film
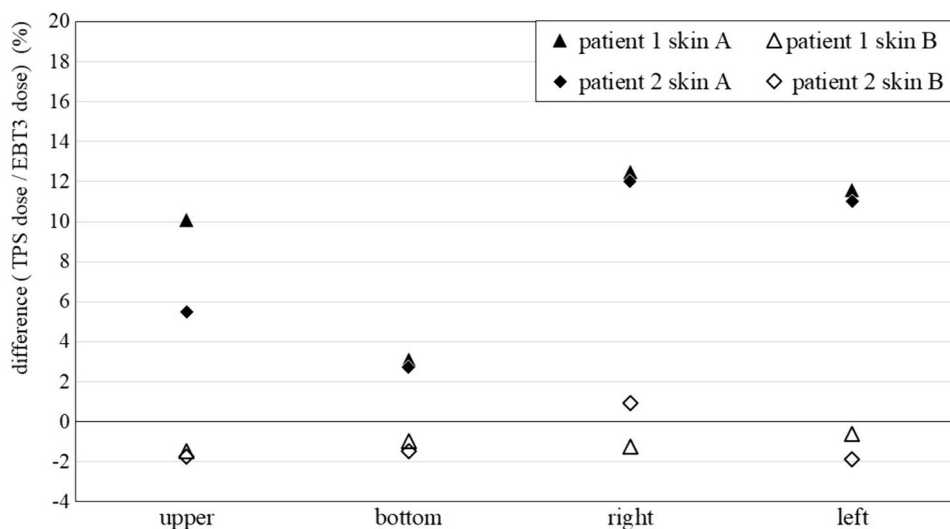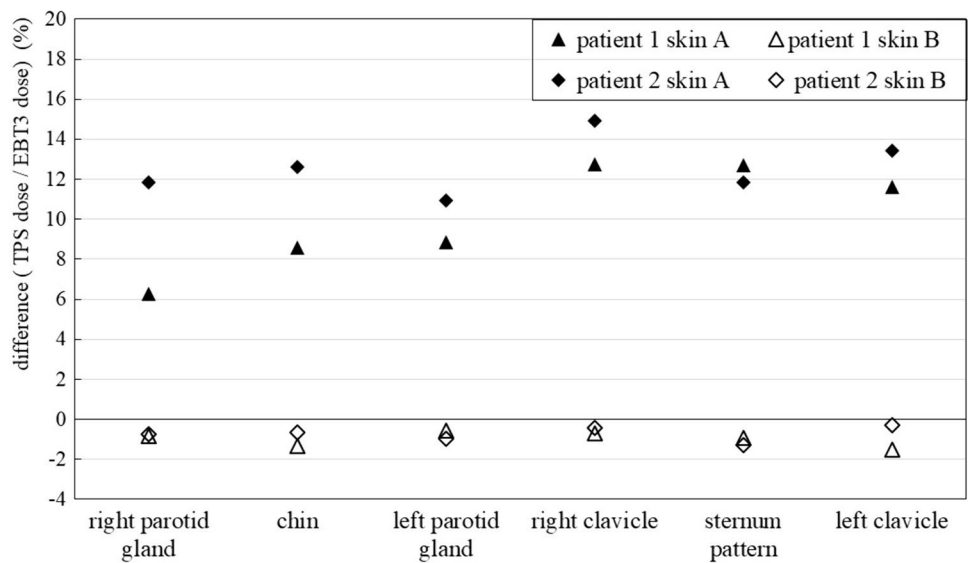
**Fig. 6** Comparison between EBT3-measured doses and TPS-calculated doses for skin A and B in anthropomorphic phantoms. Skin A is overestimated by up to 15%, whereas skin B improved the dose difference to within 2%



each 1 mm depth to the skin surface (Fig. 7a (2)). For skin B, the dose calculation began approximately 6.0 mm (Fig. 7a (3)) from the skin surface and 4.5 mm outside the external body contour (Fig. 7a (4)). In addition, the dose profile of skin B increased by approximately 250 cGy at a depth of 1 mm (Fig. 7a (5)). Similarly, patient 2 displayed different dose gradients for skin A and B. For skin A, the dose calculation began 1.5 mm outside the skin surface (Fig. 7b (1)), and the dose increased by approximately 750 cGy/mm (Fig. 7b (2)). Dose calculations for skin B began approximately 3.0 mm from the skin surface (Fig. 7b (3)) and 2.0 mm from the body contour (Fig. 7b (4)). The dose profile of skin B exhibited an increase of approximately 300 cGy for each depth of 1.0 mm (Fig. 7b (5)). Notably, the 1-mm extension of the external body contour was calculated using the calculation starting point more than 1 mm outward due to the effect of voxel resolution [11, 20].

### 3.3 Comparison between target volume and risk-organ doses

The dose differences for the skin, GTV, CTV, and PTV for skins A and B in patient 1 were 8.8%, 0.00031%, 0.00025%, and 0.00008%, respectively. The dose differences for the skin, GTV, CTV, PTV, GTVn, CTVn, and PTVn for skins A and B in patient 2 were 7.6%, −0.00015%, −0.00014%, 0.00015%, 0.00011%, 0.00018%, and 0.00019%, respectively. The dose differences for all organs at risk in patients 1 and 2 were ≤ 0.01% (Table 1).

## 4 Discussion

This study investigated the placement of skin-ring structures to improve the accuracy of skin-dose calculations in patients undergoing full-arc head and neck VMAT. In the dose comparison between EBT3 and TPS, the conventional method for skin A showed a maximum dose difference of approximately 13%, which is consistent with the results reported in previous studies [21–23]. On the other hand, skin B significantly improved the accuracy of the skin-dose calculation by approximately 2%. Notably, some studies have extrapolated EBT3 doses to accurately measure skin doses [24–26]. However, other studies on the accuracy of TPS calculations have reported low accuracy due to the omission of measurement-depth issues [11, 27–29].

There is a limit to the thickness of the skin-ring structures created by the TPS. The thickness of the skin-ring structures depends on the voxel size. In this study, the field of view was 500 mm and the matrix was $512 \times 512$. Since one pixel corresponds to 0.9765 mm, the minimum thickness of the skin-ring structure is 2 mm. However, it is not possible to further decrease the thickness of the skin-ring structures by simply adjusting their dimensions, as demonstrated in skin A. Therefore, alternative methods need to be considered. Notably, skin B has a structure that extends beyond the body contour and is not originally

**Fig. 7** **a** Dose profile of patient 1 at any position. When the external body contour is extended outward by 1 mm, the calculation starting point for skin B moved away from the skin, and the slope of the dose incident on the skin decreased. **b** Dose profile at any position of patient 2. As in Fig. 7a, the calculation starting point is farther away from the skin, and the slope of the dose incident on the skin is slower. The extension of the external body contour contributes to the dose distribution at the boundary between the air and the patient/phantom
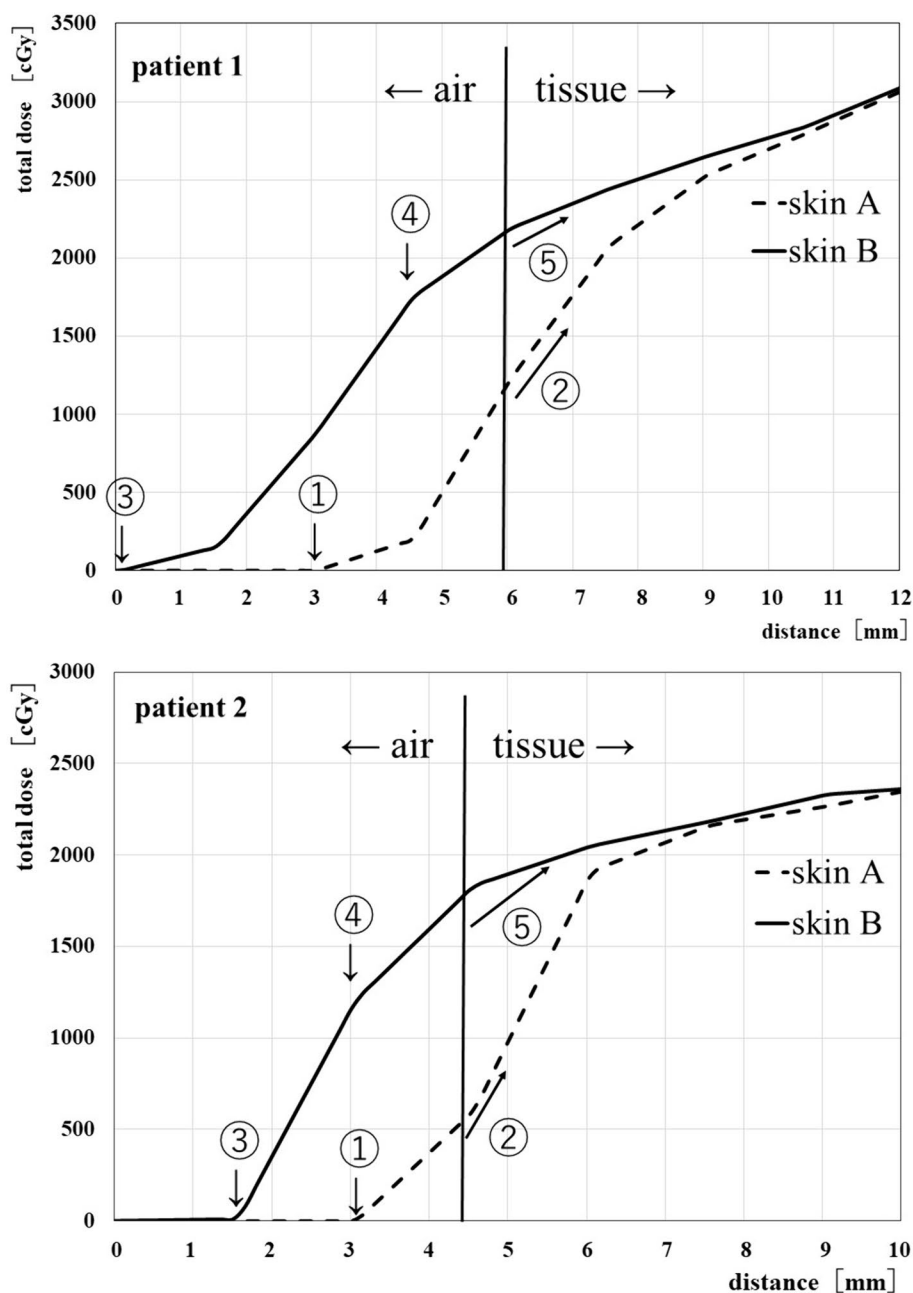
present. However, the accuracy of the model-based calculation algorithm can improve the accuracy of the calculation as it approaches the entrance. In essence, the skindose reduction is greater without a thermoplastic mask [30]. Nevertheless, in VMAT, the exit dose contributes significantly to the skin dose [15, 31]. This is another factor that improves the calculation accuracy by avoiding a sharp decline on the exit side [32, 33].

Skin B did not affect the target volume or at-risk organs, with a dose difference of $< 0.01\%$ (Table 1). This result aligns with the findings reported by Tanaka et al. [20]. This is because the build-up effect is smaller when the

effective depth is $\geq 4$ mm [30]. Another factor is that with a 360-degree rotating VMAT, even better scattering conditions can be achieved using a fixed device, such as a thermoplastic mask, "behind" the patient [31]. In addition, skin B follows the usual depth-dose percentage curve [15, 32, 33] and does not affect the target volume or risk-organ dose. To explore this further, we investigated the volume structures outlined in the TPS, such as the skin-ring structures, target volumes, and organs at risk. As shown in Fig. 7a and b, the dose profiles provide a survey of point doses at various locations. Notably, the VMAT skin doses were speckled [31], indicating that skin B doses were higher than skin A

**Table 1** Comparison between the mean doses of the target volumes and organs at risk, as well as the percentage changes, due to extension of the external body contour

(a)

Patient 1

| Structure | DVH parameter | Skin A | Skin B | {(Skin A-skin B) skin A} 100 (%) |
|---|---|---|---|---|
| Skin | $D_{mean}$ | 685.2 | 624.8 | 8.8 |
| GTV | $D_{99\%}$ | 7120.8 | 7122.4 | 0.00031 |
| CTV | $D_{99\%}$ | 7113.8 | 7115.6 | 0.00025 |
| PTV | $D_{99\%}$ | 7075.4 | 7076.0 | 0.00008 |
| GTVn | $D_{99\%}$ | – | – | – |
| CTVn | $D_{99\%}$ | – | – | – |
| PTVn | $D_{99\%}$ | – | – | – |
| Brain | $D_{mean}$ | 91.9 | 92.2 | 0.00325 |
| Brainstem | $D_{mean}$ | 209.8 | 210.3 | 0.00238 |
| Lung | $D_{mean}$ | 197.7 | 198.0 | 0.00152 |
| Spinal cord | $D_{mean}$ | 1545.2 | 1546.0 | 0.00052 |
| Rt. parotid gland | $D_{mean}$ | 1728.0 | 1729.7 | 0.00098 |
| Lt. parotid gland | $D_{mean}$ | 1736.4 | 1738.5 | 0.00121 |
| Trachea | $D_{mean}$ | 1293.6 | 1293.3 | −0.00023 |
| Brainstem PRV | $D_{mean}$ | 228.1 | 228.7 | 0.00262 |
| Spinal cord PRV | $D_{mean}$ | 1557.6 | 1558.4 | 0.00051 |
| Rt. parotid PRV | $D_{mean}$ | 1101.8 | 1104.7 | 0.00263 |
| Lt. parotid PRV | $D_{mean}$ | 1096.9 | 1100.4 | 0.00318 |

(b)

Patient 2

| Structure | DVH parameter | Skin A | Skin B | {(Skin A-skin B) skin A} 100 (%) |
|---|---|---|---|---|
| Skin | $D_{mean}$ | 869.1 | 803.2 | 7.6 |
| GTV | $D_{99\%}$ | 7112.4 | 7111.3 | −0.00015 |
| CTV | $D_{99\%}$ | 6960.3 | 6959.3 | −0.00014 |
| PTV | $D_{99\%}$ | 6772.2 | 6771.2 | −0.00015 |
| GTVn | $D_{99\%}$ | 7079.1 | 7078.3 | −0.00011 |
| CTVn | $D_{99\%}$ | 7088.2 | 7086.9 | −0.00018 |
| PTVn | $D_{99\%}$ | 7009.6 | 7008.3 | −0.00019 |
| Brain | $D_{mean}$ | 250.8 | 251.2 | 0.00159 |
| Brainstem | $D_{mean}$ | 685.4 | 685.8 | 0.00058 |
| Lung | $D_{mean}$ | 427.4 | 427.4 | 0.00000 |
| Spinal cord | $D_{mean}$ | 2049.6 | 2049.5 | −0.00005 |
| Rt. parotid gland | $D_{mean}$ | 2604.3 | 2606.2 | 0.00073 |
| Lt. parotid gland | $D_{mean}$ | 1787.6 | 1789.8 | 0.00123 |
| Trachea | $D_{mean}$ | 1943.5 | 1941.3 | −0.00113 |
| Brainstem PRV | $D_{mean}$ | 743.7 | 744.1 | 0.00054 |
| Spinal cord PRV | $D_{mean}$ | 2062.4 | 2062.2 | 0.00010 |
| Rt. parotid PRV | $D_{mean}$ | 1328.5 | 1330.8 | 0.00173 |
| Lt. parotid PRV | $D_{mean}$ | 1234 | 1236.5 | 0.00202 |

doses, in contrast to the aforementioned results. Since even slight differences in measurement points can alter the profile shape, caution is advised when examining skin doses using arbitrary profiles. In our study, we believe that arbitrary profiles are unreliable for skin-dose evaluation and that it is better to evaluate skin dose by volume.

Therefore, skin B allows for a more realistic evaluation of the surface doses obtained using EBT3.

## 5 Conclusion

This study aimed to improve the accuracy of skin-dose calculations in patients who underwent full-arc head and neck VMAT using skin-ring structures. Skin B, calculated using AXB, exhibited a dose difference of approximately 2% compared to that of EBT3. In the phantom study, skin A (with a conventional skin-ring structure) showed a dose difference of 13%, whereas skin B (new skin-ring structure) showed an improvement of approximately 10% (within 2%). In clinical cases, improvements of 8.2% and 9.2% were observed in patients 1 and 2, respectively, for skin B. Furthermore, extending the external body contour of skin B by 1 mm did not affect the dose delivered to the target or organ at risk. Overall, skin B can be used as an indicator to evaluate skin dose during the treatment-planning phase.

## Declarations

**Conflict of interest** All authors declare that they have no conflict of interest.

**Ethical approval** This study was approved by the ethics committee of Kyushu Cancer Center (2022–30) and was conducted according to the Declaration of Helsinki.

## References

1. Bozec A, Culié D, Poissonnet G, Dassonville O. Current role of total laryngectomy in the era of organ preservation. Cancers. 2020;12:584. https://doi.org/10.3390/cancers12030584.
2. Leventhal J, Young MR. Radiation dermatitis: recognition, prevention, and management. Oncology. 2017;31:885–7, 894–9. https://europepmc.org/article/med/29297172.
3. Gamez ME, Blakaj A, Zoller W, Bonomi M, Blakaj DM. Emerging concepts and novel strategies in radiation therapy for laryngeal cancer management. Cancers. 2020;12:1651. https://doi.org/10.3390/cancers12061651.
4. Kaidar-Person O, Gil Z, Billan S. Precision medicine in head and neck cancer. Drug Resist Updates. 2018;40:13–6. https://doi.org/10.1016/j.drup.2018.09.001.
5. Lalla RV, Brennan MT, GoRDon SM, Sonis ST, Rosenthal DI, Keefe DM. Oral mucositis due to high-dose chemotherapy and/or head and neck radiation therapy. JNCI Monographs. 2019;53:lgz011. https://doi.org/10.1093/jncimonographs/lgz011.
6. Lin D, Lapen K, Sherer MV, et al. A systematic review of contouring guidelines in radiation oncology: analysis of frequency, methodology, and delivery of consensus recommendations. Int J Radiat Oncol Biol Phys. 2020;107:827–35. https://doi.org/10.1016/j.ijrobp.2020.04.011.
7. Chung H, Jin H, Dempsey JF, et al. Evaluation of surface and build-up region dose for intensity-modulated radiation therapy in head and neck cancer. Med Phys. 2005;32:2682–9. https://doi.org/10.1118/1.1992067.
8. Higgins PD, Han EY, Yuan JL, Hui S, Lee CK. Evaluation of surface and superficial dose for head and neck treatments using conventional or intensity-modulated techniques. Phys Med Biol. 2007;52:1135. https://doi.org/10.1088/0031-9155/52/4/018.
9. Baba MH, Singh BK. In-vivo skin dose measurement using gafchromic EBT3 film dosimetry in the radiation therapy of Head and Neck cancers: 2DRT versus IMRT. J Radiat Res Appl Sci. 2022;15:170–4. https://doi.org/10.1016/j.jrras.2022.05.019.
10. Sheykholeslami N, Parwaie W, Farzin M, Vaezzadeh V, Geraily G. An investigation into the surface dose using eclipse treatment planning system and film dosimetry for treatment of breast cancer. Front Biomed Technol. 2023;2023(10):27–31. https://doi.org/10.18502/fbt.v10i1.11509.
11. Wang L, Cmelak AJ, Ding GX. A simple technique to improve calculated skin dose accuracy in a commercial treatment planning system. J Appl Clin Med Phys. 2018;19:191–7. https://doi.org/10.1002/acm2.12275.
12. Eclipse Photon and Electron Algorithms Reference Guide: This document provides reference information about the algorithms supported in Eclipse, version 13.6. California: Varian medical systems; 2015. 286.
13. Chiu-Tsao S, Sim S, Chan MF. The impact of patient immobilization devices on skin dose during IMRT: a radiochromic EBT film dosimetry study in phantom. Int J Radiat Oncol Biol Phys. 2008;72:S659. https://doi.org/10.1016/j.ijrobp.2008.06.346.
14. Olch AJ, Gerig L, Li H, Mihaylov I, Morgan A. Dosimetric effects caused by couch tops and immobilization devices: report of AAPM task group 176. Med Phys. 2014;41:061501. https://doi.org/10.1118/1.4876299.
15. Hadley SW. Effects of immobilization mask material on surface dose. J Appl Clin Med Phys. 2005;6:2005. https://doi.org/10.1120/jacmp.v6i1.1957.
16. Merlotti A, Alterio D, Vigna-Taglianti R, et al. Technical guidelines for head and neck cancer IMRT on behalf of the Italian association of radiation oncology-head and neck working group. Radiat Oncol. 2014;9:1–32. https://doi.org/10.1186/s13014-014-0264-9.
17. Fiorino C, Dell'Oca I, Pierelli A, et al. Simultaneous integrated boost (SIB) for nasopharynx cancer with helical tomotherapy. Strahlenther Onkol. 2007;183:497. https://doi.org/10.1007/s00066-007-1698-x.
18. Baba MH, Singh BK. In-vivo skin dose measurement using gafchromic EBT3 film dosimetry in the radiation therapy of Head and Neck cancers: 2DRT versus IMRT. J Radiat Res Appl Sci. 2020;15:170–4. https://doi.org/10.1016/j.jrras.2022.05.019.
19. Dreindl R, Georg D, Stock M. Radiochromic film dosimetry: considerations on precision and accuracy for EBT2 and EBT3 type films. Z Med Phys. 2014;24:153–63. https://doi.org/10.1016/j.zemedi.2013.08.002.
20. Tanaka Y, Monzen H, Matsumoto K, Inomata S, Fuse T. Dose distribution comparison in volumetric-modulated arc therapy plans for head and neck cancers with and without an external body contour extended technique. Reports Pract Oncol Radiother. 2019;24(6):576–84. https://doi.org/10.1016/j.rpor.2019.09.003.
21. Avanzo M, Drigo A, Kaiser SR, et al. Dose to the skin in helical tomotherapy: results of in vivo measurements with radiochromic films. Physica Med. 2013;29:304–11. https://doi.org/10.1016/j.ejmp.2012.04.004.

22. Mahur M, Singh M, Semwal M K, Gurjar O P. Evaluation of surface dose calculations using monaco treatment planning system in an indigenously developed head and neck phantom. Medical Journal of Dr. DY Patil University. 2023. https://journals.lww.com/mjdy/toc/2023/16050.

23. Giuliano A, Ravaglia V. 149. Skin dose in radiotherapy: results of in vivo measurements with Gafchromic EBT3 films. Phys Med Eur J Med Phys. 2018;56:156–7. https://doi.org/10.1016/j.ejmp.2018.04.160.

24. Devic S, Seuntjens J, Abdel-Rahman W, et al. Accurate skin dose measurements using radiochromic film in clinical applications. Med Phys. 2006;33:1116–24. https://doi.org/10.1118/1.2179169.

25. Chiu-Tsao ST, Chan MF. Photon beam dosimetry in the superficial buildup region using radiochromic EBT film stack. Med Phys 36(6Part1). 2009;36:2074–83. https://doi.org/10.1118/1.3125134.

26. Kern A, Bäumer C, Kröninger K, et al. Determination of surface dose in pencil beam scanning proton therapy. Med Phys. 2020;47:2277–88. https://doi.org/10.1002/mp.14086.

27. Fleckenstein J, Eschler A, Kremp K, Kremp S, Rübe C. Dose distribution and tumor control probability in out-of-field lymph node stations in intensity modulated radiotherapy (IMRT) vs 3D-conformal radiotherapy (3D-CRT) of non-small-cell lung cancer: an in silico analysis. Radiat Oncol. 2015; 10: 1–7. https://rdcu.be/dose6.

28. Joosten A, Matzinger O, Jeanneret-Sozzi W, Bochud F, Moeckli R. Evaluation of organ-specific peripheral doses after 2-dimensional, 3-dimensional and hybrid intensity modulated radiation therapy for breast cancer based on Monte Carlo and convolution/superposition algorithms: implications for secondary cancer risk assessment. Radiother Oncol. 2013;106:33–41. https://doi.org/10.1016/j.radonc.2012.11.012.

29. Lu CC, Wang FN, Lin HH, Hsu CH, Lin JP, Lai LH. Dosimetric measurement of testicular dose for colorectal cancer using optically-stimulated luminescent dosimeters in radiotherapy. Radiat Phys Chem. 2020;172:108792. https://doi.org/10.1016/j.radphyschem.2020.108792.

30. Kry SF, Smith SA, Weathers R, Stovall M. Skin dose during radiotherapy: a summary and general estimation technique. J Appl Clin Med Phys. 2012. https://doi.org/10.1120/jacmp.v13i3.3734.

31. Lowther NJ, Marsh SH, Louwe RJ. Dose accumulation to assess the validity of treatment plans with reduced margins in radiotherapy of head and neck cancer. Phys Imag Radiat Oncol. 2020. https://doi.org/10.1016/j.phro.2020.05.004.

32. Velec M, Waldron JN, O'Sullivan B, et al. Cone-beam CT assessment of interfraction and intrafraction setup error of two head-and-neck cancer thermoplastic masks. Int J Radiat Oncol Biol Phys. 2010;76:949–55. https://doi.org/10.1016/j.ijrobp.2009.07.004.

33. Penoncello GP, Ding GX. Skin dose differences between intensity-modulated radiation therapy and volumetric-modulated arc therapy and between boost and integrated treatment regimens for treating head and neck and other cancer sites in patients. Med Dosim. 2016;41:80–6. https://doi.org/10.1016/j.meddos.2015.09.001.